COMMUNICATION

Check for updates

Bio-based derived carbon materials for permittivity metamaterials: dual efficacy of electromagnetic wave protection and Joule heating†

Chenchen Wang, Xiuyi Lin, Chuanshuang Hu,* Yao Ding, Zhuoqun Wang, Yonghui Zhou,* Xi Lin and Jiangtao Xu [ID] *

Epsilon-negative metamaterials (ENMs) have attracted extensive research interest due to their unique physical properties and advanced applications in electromagnetic fields. In this study, carbonized wood@Prussian blue derivative (CW@PBD) metacomposites were fabricated from a carbonized wood@Prussian blue analogue (PBA). By varying the PBD content, the negative permittivity constant of the supercomposite can be tuned between -45 and -20. The CW@PBD metacomposites exhibit outstanding electromagnetic interference (EMI) shielding effectiveness of 39 dB, with a significant 40.9% increase in absorption loss (SE_A). Notably, as the PBD content rises, the CW@PBD composites transform from EMI shielding to microwave absorption. The minimum reflection loss (RL_{min}) reaches -49.2 dB, and the effective absorption bandwidth (EAB) covers the entire X-band. Moreover, the CW@PBD metacomposites demonstrate remarkable Joule heating capabilities, achieving a steady-state saturation temperature (T_s) of 255.68 °C at 3 V. This research offers a promising approach for synthesizing ENMs, endowing biomass-based materials with desired functions for electromagnetic applications.

New concepts

Synthesis route for epsilon-negative metamaterials: The synthesis of biomass metamaterials provides a new approach to fabricating ε-negative metamaterials (ENMs). The graphitization process of biomass materials was induced by using wood@Prussian blue analogues as precursors. Self-construction of over-permeable materials during the graphitization transition of natural biomass carbon materials provides a simple and potentially scalable approach to fabricating ENMs, unlike the complex and expensive synthetic routes in previous studies. This new synthetic concept paves the way for wider applications of ENMs in various fields. By controlling the content of blue analogues, the negative permittivity constant of the metamaterials can be precisely tuned, which is a significant departure from traditional non-tunable or difficult-to-tune metamaterial systems.

1. Introduction

Electromagnetic metamaterials exhibiting negative permittivity have garnered significant interest due to their distinctive physical properties. These unique characteristics include the inverse Cherenkov radiation effect, the inverse Doppler effect, inverse Snell's law refraction, and negative refraction.[1,2] A key attribute of such synthetic materials is their epsilon-negativity, which endows them with exceptional electromagnetic responses.

These responses hold considerable promise for a wide array of applications, spanning from aerospace engineering to communications, electromagnetic interference (EMI) shielding, and microwave absorption.[3,4]

Typically, negative permittivity is observed when the frequency of an external electromagnetic field is lower than the plasma frequency, enabling electron plasma oscillations.[5,6] Consequently, metals are frequently used to fabricate epsilon-negative metamaterials (ENMs) to achieve negative permittivity. Current research on ENMs predominantly explores metallic materials and metal-doped ceramic materials.[7–9] It has been demonstrated that the generation of plasma oscillation is related to a continuous conductive network within the ENMs. However, establishing a metal conductive network requires a significant concentration of metal particles to form a network capable of inducing negative permittivity.[4,7,10] Negative permittivity is also observed in percolative composites, carbonaceous fillers, and conductive polymers.[3,11] Forming percolation networks using conductive carbonaceous fillers in these composites is pivotal for achieving negative permittivity. Nevertheless, constructing a percolative network in polymer composites is complex and inefficient. Therefore, developing self-constructed

Key Laboratory of Advanced Materials for Facility Agriculture, Ministry of Agriculture, College of Materials and Energy, South China Agricultural University, Guangzhou, 510642, China. E-mail: cshu@scau.edu.cn, y.zhou@scau.edu.cn, jiangtao.xu@scau.edu.cn

percolating material systems that can achieve negative permittivity by carbonizing natural biomass materials is highly desirable.

Wood, a natural, sustainable, renewable resource, offers cost-effective and environmentally friendly materials with biodegradability and a unique porous structure.[12] Its chemical composition is predominantly cellulose, hemicellulose, and lignin, which, upon undergoing graphitization during oxygen-free high-temperature carbonization, transform into carbonized wood (CW) with electrical conductivity. Forming a conducting network is essential for achieving negative permittivity, making carbon materials with self-assembled carbon networks promising for developing ENMs. In recent years, CW has been gradually applied to EMI shielding.[13] Natural wood carbonized at 1000 °C at 3 mm thickness shows an average EMI shielding effectiveness (SE) of 26.42 or 44.2 dB.[14,15] Excellent EMI shielding or microwave absorption performance can effectively prevent the harm caused by EMW radiation to human body and electronic equipment. At the same time, for designing electronic equipment in cold areas, we should take into account both electromagnetic waves and low temperature environment damage to outdoor electronic equipment. Therefore, the development of electromagnetic protective equipment with Joule heating capability is crucial. A Joule heater fabricated from CW has been reported to reach a steady-state saturation temperature (T_s) of up to 100 °C at a voltage of 2.5 V,[16] or a range of 28.0 to 83.5 °C when subjected to a voltage between 0.5 and 2.0 V.[14,17]

Despite the abundance of carbonized materials, research on negative permittivity within this domain remains scarce. Concurrently, most existing studies on preparing materials with negative permittivity have primarily focused on their radio frequency (RF) range characteristics. In a study, Wang *et al.* demonstrated that high-temperature carbonization of cellulose microcrystals (CMC) led to the formation of self-assembled percolation networks, which in turn altered the conductive mechanism and resulted in a shift to negative permittivity.[18] Furthermore, Guo's team reported on carbon nanofibers (CNFs) exhibiting negative permittivity in the microwave frequency band, which were derived from cellulose nanofibers through a process of freeze-drying and subsequent high-temperature carbonization.[11] However, their study did not extend to exploring the practical applications of these materials in EMI shielding or other relevant fields. Consequently, there is a pressing need for further research to investigate the negative permittivity of CW in the microwave frequency range. Exploring the potential applications of ENMs in this frequency band is of considerable interest and significance.

In this study, carbonised wood (CW@PBD) with negative dielectric constant properties was prepared by carbonising wood loaded with PBA nanoparticles (PBA NPs). The negative permittivity is analyzed employing the Drude model. The relationship between absorbing loss (SE$_A$), reflecting loss (SE$_R$), conductivity, and impedance matching was elucidated through a series of derived equations. As expected, CW@PBD$_{15}$ and CW@PBD$_{25}$ metacomposites, endowed with negative permittivity, demonstrated superior EMI shielding effectiveness.

Moreover, the synthesized CW@PBD$_{25}$ metacomposites exhibited remarkable Joule heating characteristics. This work provides new ideas for the preparation of high-performance EMI shielding materials.

2. Experimental

2.1. Materials

Poplar wood (*Populus* L., Henan, China) was used for the experiment. Potassium ferricyanide (K$_3$[Fe(CN)$_6$]·6H$_2$O), cobalt nitrate hexahydrate (Co(NO$_3$)$_2$·6H$_2$O), trisodium citrate dihydrate (Na$_3$C$_6$H$_5$O$_7$·2H$_2$O), sodium chlorite (80%, NaClO$_2$), and acetic acid (99%) were acquired from Shanghai Aladdin Biochemical Technology Co., Ltd (China). Deionized (DI) water was prepared in the laboratory. All the reagents used in this experiment were analytically pure.

2.2. Synthesis of Co–Fe PBAs

Firstly, 0.6 mmol Co(NO$_3$)$_2$·6H$_2$O and 0.9 mmol Na$_3$C$_6$H$_5$O$_7$·2H$_2$O were dispersed in 20 mL of DI water by ultrasonication for 30 min. Secondly, 0.4 mmol K$_3$[Fe(CN)$_6$]·6H$_2$O was dissolved in 20 mL of DI water. Subsequently, the obtained solution was thoroughly mixed with the previous solution. Afterward, the mixture solution was allowed for low-speed mixing at room temperature for 12 h. Then, the obtained products were repeatedly centrifugally washed with DI water and absolute ethanol. Finally, Co–Fe PBAs NPs were obtained after drying for 24 h.

2.3. Preparation of CW@PBD

The poplar wood veneers were treated with 8 wt% of NaClO$_2$ with acetate buffer solution (pH 4.6) at 80 °C for 6 h. The extracted samples were carefully washed with deionized water to remove extra chemicals. The delignified wood samples were freeze-dried for 48 h to obtain wood aerogels. Then, the Co–Fe PBA NPs were ultrasonically dispersed in DI water and configured into dispersions with concentrations of 15 mg ml^{-1}, 25 mg ml^{-1}, and 35 mg ml^{-1}. Wood aerogel@PBA composites with different loadings were prepared by impregnation at a pressure of 1 MPa for 3 h. Subsequently, the composites were dried at 60 °C for 24 h.

The wood aerogel@PBA composites were pre-carbonized at 300 °C for 2 h and then carbonized at 1000° for 3 h at a heating rate of 5 °C min^{-1} under nitrogen in a tube furnace to obtain a carbonized wood@PBA derivative (CW@PBD). CW@PBD prepared with different impregnating concentrations is named CW@PBD$_{15}$, CW@PBD$_{25}$, and CW@PBD$_{35}$, respectively. Additionally, pure CW was prepared as a comparison sample using the same methodology.

2.4. Characterization

The morphological structure was observed using scanning electron microscopy (SEM, EVO18, Zeiss, Germany). The PBD content of CW@PBD is obtained by thermogravimetric analysis (TGA, TG209F1LibraTM, Germany) in the air atmosphere at 800 °C. The chemical composition and structure of samples

were identified by X-ray photoelectron spectroscopy (XPS, Thermo Scientific K-Alpha, America). The crystal structure was obtained by X-ray diffraction (XRD) at $5°$ min^{-1} with CuKα ($\lambda = 0.15405$ nm) irradiation (Ultima IV, Japan). Raman spectroscopy was conducted using a confocal Raman spectrometer (Alpha300R, Germany) with a wavelength of 532 nm. Conductivity was measured with a four-probe instrument (ST2258C, China). The surface temperature change of specimens was recorded using a thermal infrared camera (Fluke TIS75, America). The oxygen vacancies were detected by electron paramagnetic resonance (EPR, EMXnano, Bruker, USA). The scattering parameters (S11 and S21), complex permittivity (ε' and ε''), and permeability (μ' and μ'') were measured using a vector network analyzer (VNA, E5080B, Agilent, USA) in the frequency range of 8.2–12.4 GHz (X band) using the waveguide method, and the tested CW@PBD was processed into a regular rectangle block with a three-dimensional size of $22.86 \times 10.16 \times 3$ mm. The corresponding reflection coefficient (R), penetration coefficient (T), absorption coefficient (A), reflection loss (SE_R), absorption loss (SE_A), and total EMI (SE_T) were calculated using eqn (S1)–(S6) (ESI†).[15,17]

3. Results and discussion

3.1. Preparation and characterization of CW@PBD

The preparation process of the wood@Prussian blue derivative (CW@PBD) is schematically shown in Fig. 1. Natural wood underwent delignification to enhance its pore structure, forming a wood aerogel. The synthesized Prussian blue analogue nanoparticles (PBA NPs) were dispersed in water to form dispersions of different concentrations (15 mg ml^{-1}, 25 mg ml^{-1},

and 35 mg ml^{-1}). Pressurized impregnation was employed to infuse PBA NPs into the porous skeletal structure of the wood aerogel. Subsequently, CW@PBD was successfully prepared by high-temperature carbonization under a nitrogen atmosphere. The presence of trace quantities of metallic particles during the carbonization process can facilitate the graphitization of CW, thereby enhancing the degree of graphitization.[19,20] Consequently, by modulating the loading of PBD nanocubes, CW@PBD can be achieved with varying degrees of graphitization.

The microscopic morphologies of CW@PBD are shown in Fig. S1 (ESI†) and Fig. 2. As illustrated in Fig. S1a–c (ESI†), the nano-sized PBAs were successfully attached to the skeletal structure of the wood aerogel. After the high-temperature carbonization process, CW@PBD preserves the honeycomb porous structure of the original wood. Meanwhile, the PBD NPs maintain their original morphology attached to the porous structure of the CW (Fig. 2g–i). The EDS analysis of the CW@PBD cross-section, as illustrated in Fig. S1 (ESI†), confirms the effective integration of the nano-PBD into the porous framework of the CW. The backbone structure of CW is instrumental in creating an efficient three-dimensional conductive network, which significantly enhances the electromagnetic interference (EMI) shielding performance.[19] Additionally, the porous architecture is conducive to the efficient reflection and scattering of electromagnetic waves (EMWs), thereby contributing to the overall EMI shielding effectiveness.[21]

TG was employed to assess the thermal stability of composite materials and determine the proportion of each constituent. Fig. 3a displays the TG curves of CW@PBD. In the temperature range of 100 °C to 300 °C, a slight weight loss is observed across all samples due to the evaporation of crystalline water, as indicated
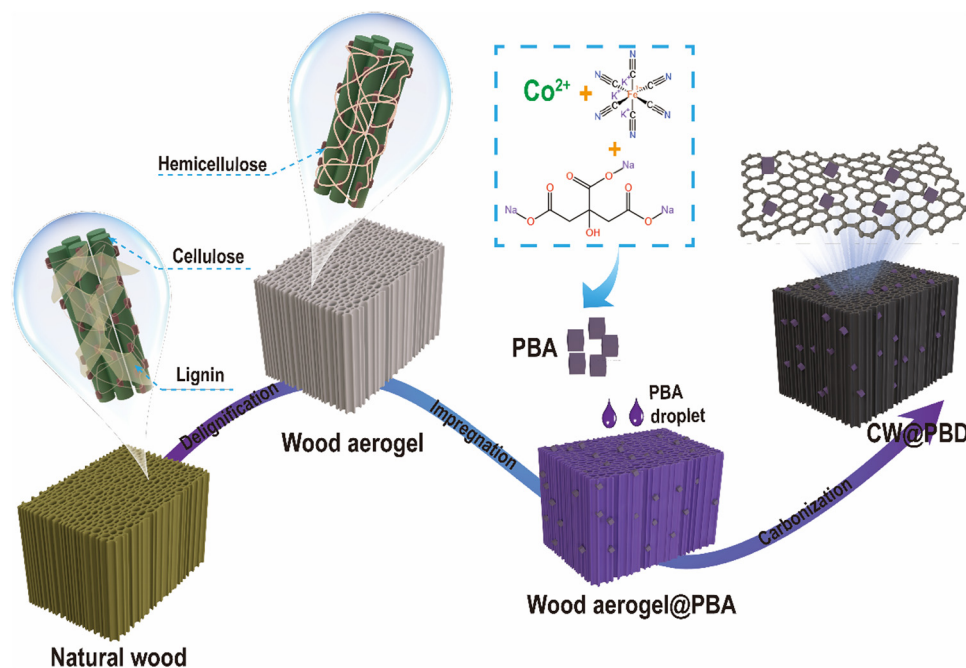

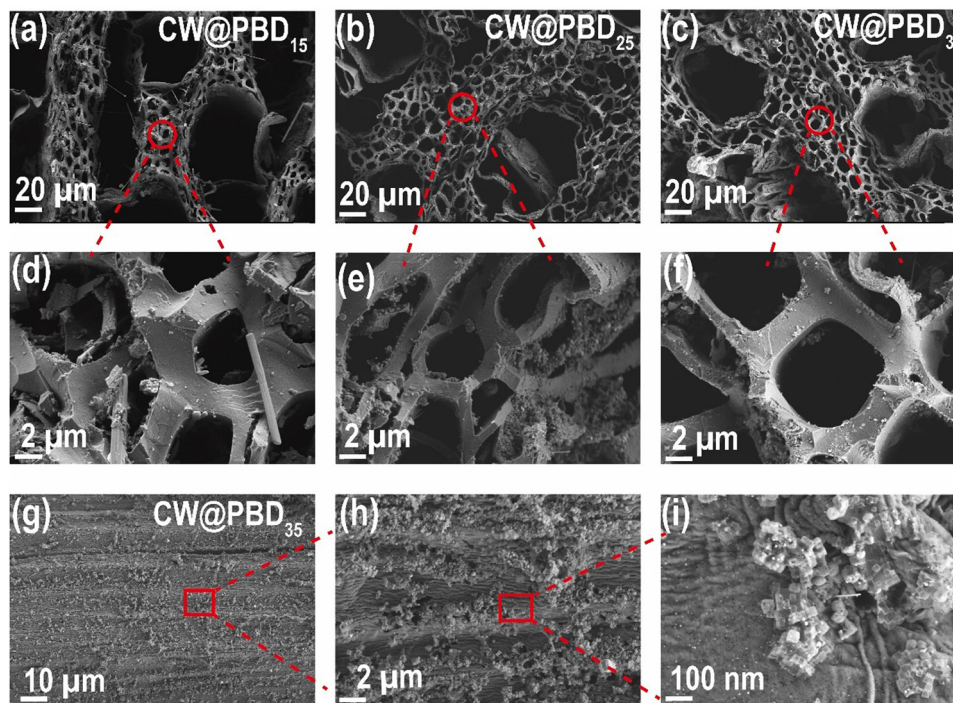Fig. 1 The schematic illustration of the CW@PBD formation process.

Fig. 2 Microscopic morphology of CW@PBD. (a)–(f) Cross-sections of CW@PBD with different PBD contents and (g)–(i) micro-morphology of the CW@PBD$_{35}$ longitudinal section.

by a downward trend in the curves. The weight of the composites remains stable up to 350 °C, signifying the excellent thermal stability of CW@PBD. Beyond 350 °C, the TG curve exhibits a sharp decline, corresponding to a significant mass loss in the composite. This is predominantly due to the oxidation of amorphous carbon, which initiates at approximately 350 °C. As the carbon is oxidized and removed, the residual product consists solely of CoFe$_2$O$_4$, leading to a substantial mass loss and a rapid decrease. The remaining mass of CW@PBD-x (x = 15, 25, 35) composites is 7.85 wt%, 9.99 wt% and 10.86 wt%, respectively. The loading amount of PBD nanocubes can be estimated according to the formula[22]

$$\text{wt\% (PBD)} = \frac{m_R}{m_I} \times \frac{M_{Fe} + M_{Co}}{M_{CoFe_2O_4}} \qquad (1)$$

where m_I is the original weight of the composite, and m_R is the residual weight of the composite. The PBD contents of CW@PBD composites are 5.1 wt%, 6.9 wt% and 7.5 wt%, respectively.

X-ray photoelectron spectroscopy (XPS) was utilized to elucidate the elemental compositions and valence states of CW@PBD. As illustrated in Fig. 3b, the C, O, Co, and Fe elements have been selected to distinguish the elemental valence states of CW@PBD. The four peaks of C 1s can be found at around 284.8 eV (C–C/C=C), 285.97 eV (C–N), 286.07 eV (O–C=O), and 288.87 eV (C–O).[23] In addition, the high-resolution O 1s spectrum (Fig. 3e) of CW@PBD is deconvoluted into three peaks at 531.93 eV (O–C=O), 533.70 eV (C=O), and 535.4 eV (H$_2$O).[24] Simultaneously, the peak at 530.7 eV is related to oxygen vacancies, illustrating the presence of oxygen vacancy defects.[25] The presence of oxygen vacancies

was further characterized using EPR. As shown in Fig. 3 and Fig. S2b (ESI†), CW and CW@PBD$_{25}$ exhibited EPR signals at g = 2.002, which demonstrated the existence of oxygen vacancies.[26] Compared with CW, CW@PBD$_{25}$ displayed a stronger EPR signal, which indicated an increase in oxygen vacancies in the load of PBD NPs (Fig. 3f). Oxygen vacancies have been demonstrated to facilitate the generation of dipole polarization, thereby improving the absorption performance of EMWs.[27] The Fe 2p spectrum (Fig. S2a, ESI†) exhibits seven peaks located at about 721.90 eV (2p$_{1/2}$), 710.32 eV and 724.3 eV (Fe^{2+} 2p$_{3/2}$ and 2p$_{1/2}$), 714.20 eV and 727.0 eV (Fe^{3+} 2p$_{3/2}$ and 2p$_{1/2}$), and 719.30 eV and 734.40 eV (Sat. 2p$_{3/2}$ and 2p$_{1/2}$),[28] respectively. The Co 2p spectrum (Fig. 3d) shows four peaks at about 785.90 eV and 797.10 eV (Co^0), and 781.70 eV and 800.30 eV (Co^{2+}),[29] respectively. The above analysis further indicates that the PBD NPs were successfully loaded in CW.

3.2. Effect of PBD NPs on the graphite structure of CW@PBD

The crystal structures of the PBA NPs and CW@PBD were characterized by XRD to investigate the influence of PBA on the graphite structure evolution. As shown in Fig. S3a (ESI†), the diffraction peaks at 17.7°, 25.1°, 36.0°, 43.4°, 43.9°, and 52.0° of CoFe-PBA NPs (JCPDF#31-1000) were successfully detected. After high-temperature carbonization, CW exhibited two characteristic peaks at ∼23° and ∼44° (Fig. 4a), which correspond to the (002) and (100) crystal planes within the graphite structure. XRD analysis indicates that the graphite microcrystals dispersed in an amorphous carbon matrix. In contrast to pristine CW, the d(002) crystal plane diffraction peaks of CW@PBD$_{15}$ and CW@PBD$_{25}$ are shifted to 26.1° and
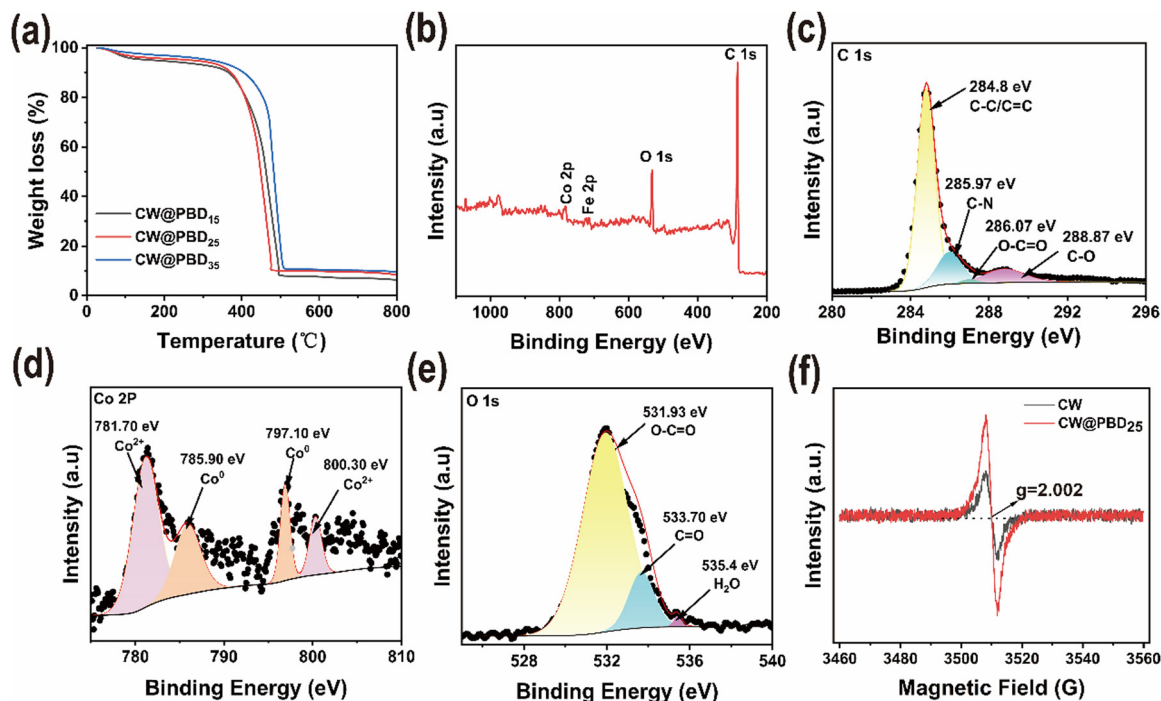
Fig. 3 (a) TG curves of CW@PBD, (b) XPS spectra for the survey spectrum, (c) C 1s, (d) Co 2p, (e) O 1s, and (f) EPR spectra of CW@PBD$_{25}$.
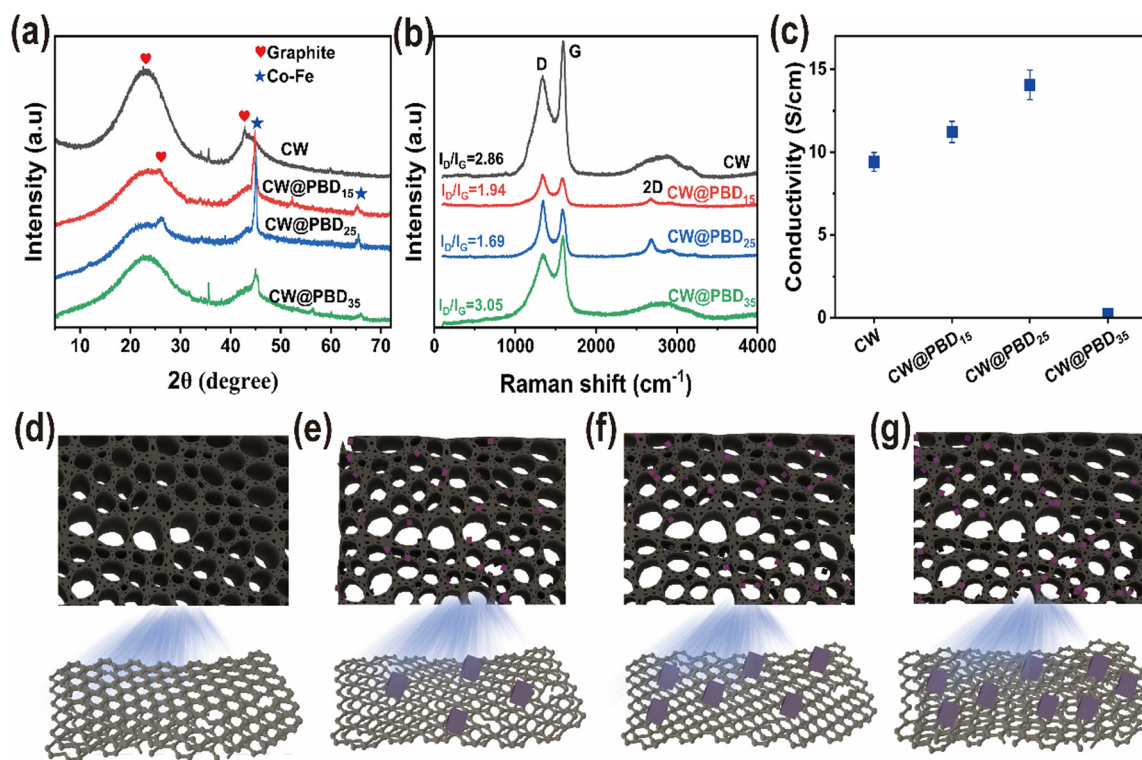

Fig. 4 (a) XRD spectra of CW and CW@PBD, (b) Raman spectra of CW and CW@PBD, (c) conductivity, and (d)–(g) schematic diagrams of the graphite structure of CW and CW@PBD.

26.3°, respectively. The presence of PBD NPs in trace amounts facilitates the crystallization of the carbon component, resulting in the formation of a hexagonal graphite structure.[30] The altered

graphite crystal structure suggests that CW@PBD$_{15}$ and CW@PBD$_{25}$ exhibit a higher degree of graphitization, conducive to enhanced conductivity. Interestingly, the crystal structure of

CW@PBD$_{35}$ did not become more pronounced with the increase in the PBD NP content. This phenomenon can be attributed to the fact that graphitized carbon impedes the incorporation of PBD NPs into its lattice, thereby diminishing the catalytic impact on the carbon crystallization process.[31]

To further elucidate the effect of PBD loading on the graphite structure, Raman spectroscopy was performed on both CW and CW@PBD composites (Fig. 4b). All spectra exhibit characteristic features of graphitized carbon materials, displaying two prominent Raman bands: the D band around 1339 cm^{-1}, which signifies the presence of disordered carbon, and the G band at 1599 cm^{-1}, indicating the presence of graphite-like structures.[32,33] The ratio of the integrated area of the D band to that of the G band (I_D/I_G) value usually serves as a metric for assessing the degree of graphitization in carbon materials. A lower I_D/I_G value represents a high graphitization grade, implying conduction loss improvement. The I_D/I_G values of samples are presented in Fig. 4b. The I_D/I_G values indicate that the addition of the PBD NPs facilitates the graphitization of the composites during the carbonization process, aligning with the XRD findings. Notably, this result appears to contradict the increase in oxygen vacancy defects as observed by XPS and EPR. This discrepancy can be attributed to the differing sensitivities of the two characterization tools to various defect types. The decline in I_D/I_G does not refute the enhancement of oxygen vacancies. Oxygen vacancies are classified as localized chemical defects, the formation of which is closely related to the high-temperature decomposition of oxygen-containing groups (e.g., C–O, C=O).[34] The growth of graphite microcrystals can be estimated based on the I_D/I_G values, as per the equation provided below (2):[19]

$$L_a \text{ (nm)} = (2.4 \times 10^{-10}) \times \lambda_I^4 \times (I_D/I_G)^{-1} \qquad (2)$$

where λ_I is the laser wavelength. Fig. S2c (ESI†) illustrates the correlation between I_D/I_G and the size of graphite grains (L_a). There is a direct proportionality between L_a and the degree of graphitization. These findings provide further evidence that trace amounts of PBD NPs can play a role in the induction of graphitic carbon crystallization. Moreover, the larger graphite crystallite size observed in CW@PBD$_{15}$ and CW@PBD$_{25}$ indicated reduced grain boundaries and edge defects on the carbon lattice, resulting in a diminished defect density. Additionally, CW@PBD$_{15}$ and CW@PBD$_{25}$ exhibit a 2D peak at 2692 cm^{-1}, indicating the stacking of a few graphite layers.[35] As shown in Fig. S3 (ESI†), both the high 2D to G peak intensity ratios (0.5–0.86) confirm that CW@PBD$_{15}$ and CW@PBD$_{25}$ feature a few-layered structure.[36]

The current tends to flow in the thinner surface of the conductive sample, so the graphite structure with fewer layers is more favorable for forming efficient conductive pathways. Consequently, samples with reduced graphite layer stacking exhibit enhanced conductivity (Fig. 4g). The conductivity of CW@PBD$_{15}$ and CW@PBD$_{25}$ is 11.2 S cm^{-1} and 14.1 S cm^{-1}, representing a 19.1% and 50% increase compared to CW (9.4 S cm^{-1}). As mentioned above, the increase in conductivity is attributed to the change in graphite structure. To offer a more comprehensive understanding, a schematic representation of the graphite structure in CW@PBD composites with varying PBD NP contents is presented in Fig. 4d–g. The pristine CW exhibits a lower degree of graphitization and a higher number of graphite layer stacking layers. Following loading trace amounts of PBD NPs, the graphitic carbon is induced to crystallize during the carbonization process, forming a graphitic structure with a few stacked layers. This structural change facilitates the movement of charge carriers and thus enhances conductivity. However, an increased loading of PBD nanocubes does not further promote the formation of graphitic carbon. Conversely, it hinders the graphitization process, significantly reducing the conductivity of CW@PBD$_{35}$.

3.3. Negative permittivity behavior of CW@PBD

CW@PBD exhibits varying graphite structures at different PBD loadings, which likely confer distinct electrical properties. Therefore, the permittivities in CW, CW@PBD$_{15}$, CW@PBD$_{25}$, and CW@PBD$_{35}$ have been comprehensively investigated. The real permittivity (ε') of CW and CW@PBD was obtained and is shown in Fig. S4 (ESI†). Positive permittivity from 8.2 to 12.4 GHz was observed in CW and CW@PBD$_{35}$. CW has a dielectric behavior of typical dielectrics, where the positive values of ε' decrease with increased frequency due to the leakage conductance.[37] In CW@PBD$_{35}$, the reduced conductivity and the consequent mitigation of the leakage conductivity phenomenon result in minimal variation of ε' with frequency. Interestingly, CW@PBD$_{15}$ and CW@PBD$_{25}$ exhibited a negative permittivity following high-temperature carbonization when loaded with a trace quantity of PBD NPs. The negative permittivity of CW@PBD$_{15}$ and CW@PBD$_{25}$ metacomposites is observed in the whole X-band, as depicted in Fig. 5a. Generally, the interplay between the plasma oscillations of delocalized charge carriers and the polarization of localized charge carriers is responsible for the emergence of negative permittivity in materials.[38]

It is reported that the negative permittivity is correlated with the formation of continuous conduction networks in the system, as well as the conductivity of materials.[37] According to the Drude model, the negative permittivity of conductive materials can be declared as follows:[38]

$$\varepsilon' = 1 - \frac{\omega_p^2}{\omega^2 + \omega_\tau^2} \qquad (3)$$

$$\omega_p = \sqrt{\frac{n_{eff} e^2}{m_{eff} \varepsilon_0}} \qquad (4)$$

where ω_p represents the angular plasma frequency, n_{eff} and m_{eff} represent the effective density and the effective mass of the electrons, ω_τ denotes the damping factor of the electron collision, ε_0 is the vacuum permittivity, and e represents the electron charge (1.6×10^{-19} C). The dispersion of ε' is well-fitted by the Drude model and the obtained reliability factors ($R^2 = 0.99$). This obedience reveals the negative permittivity can be attributed to plasma oscillations of free electrons, and variation in the value of the negative permittivity comes from
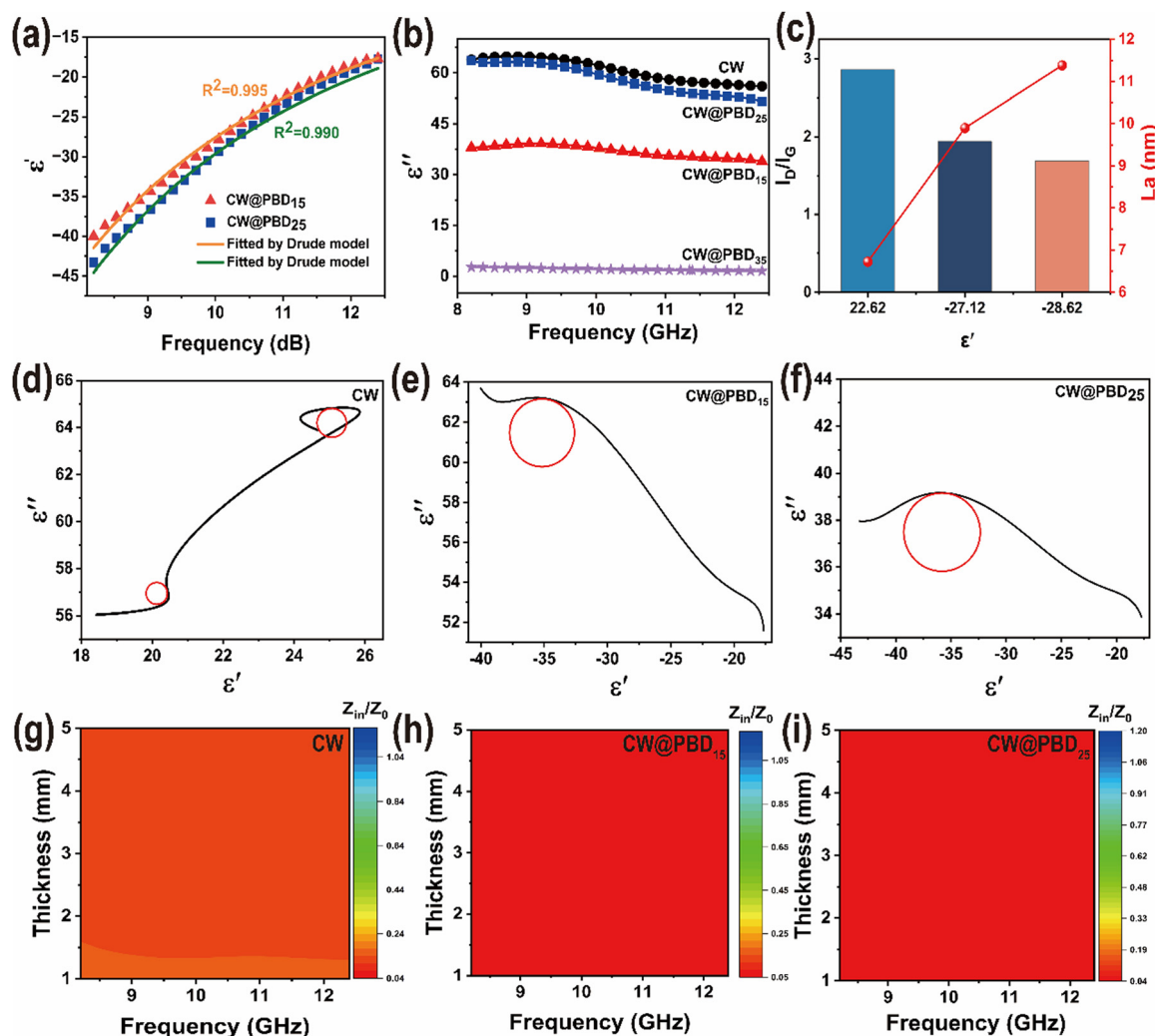
Fig. 5 (a) Real permittivity of CW@PBD, (b) imaginary permittivity of CW@PBD, (c) relationship between real permittivity, I_D/I_G, and L_a, (d)–(f) Cole–Cole curves of CW@PBD, and (g)–(i) impedance matching of CW@PBD.

the different carrier concentrations of CW@PBD$_{15}$ and CW@PBD$_{25}$ with distinct graphitization degrees. The increase in conductivity also proves the observation. Based on this, the relationship between the negative permittivity of the material and graphite defect density/particle size is further elucidated. As shown in Fig. 5c, the reduction of graphite defects effectively decreases the probability of electron scattering in the material, thereby enhancing carrier mobility and conductivity.[39] This strengthens the plasmon resonance effect, leading to a gradual increase in the absolute value of ε'. Concurrently, an increase in graphite particle size facilitates the formation of few-layer thin graphite structures. Delocalized electrons can move rapidly across these thin graphite layers,[6] which elevates the effective electron density within the material and further amplifies the negative permittivity response. When the value of ω_p exceeds the electric field frequency (ω), the dielectric constant of the material exhibits a negative value.[3] Thus, the tunable permittivity behavior essentially depends on the modulation of the internal carrier state within the materials.

The frequency dispersions of the imaginary permittivity (ε'') of CW, CW@PBD$_{15}$, CW@PBD$_{25}$, and CW@PBD$_{35}$ are depicted in Fig. 5b, where ε'' represents the assessment of the dielectric loss capability. For the prepared CW and CW@PBD, the dielectric loss mainly consists of conductivity loss (ε''_c), interfacial polarization loss (ε''_p), and dipole polarization loss (ε''_d) (eqn (S7), ESI†).[40] The CW exhibits the highest ε'', which is primarily attributable to an increased prevalence of defects in the graphite layer, leading to augmented polarization loss. The addition of a modest quantity of PBD results in a more pronounced decline in ε'' with rising frequency. The following equation represents the conductivity loss (eqn (S8), ESI†).[41] The ε'' decreases with increasing frequency after 10 GHz (Fig. 5b). This indicates that dielectric losses in composites above 10 GHz are predominantly conductive losses.

The polarization relaxation deduced from CW and CW@PBD composites can be verified by the Cole–Cole diagram derived from the Debye theory (eqn (S9), ESI†). Fig. 4a shows the Cole–Cole curve of CW, CW@PBD$_{15}$, and CW@PBD$_{25}$.

Two Cole–Cole semicircles appear in CW, while only one semicircle is in CW@PBD$_{15}$ and CW@PBD$_{25}$. This indicates that there are multiple polarization chirps in CW.[40] However, the Cole–Cole semicircle observed in CW@PBD$_{15}$ and CW@PBD$_{25}$ exhibits a larger radius, and this reveals a greater internal polarization loss capability.[42] Meanwhile, the Cole–Cole curves of CW@PBD$_{15}$ and CW@PBD$_{25}$ have straight tails (Fig. 5e and f), indicating that there is significant transmission loss in the composites. This is consistent with the above analysis of the negative permittivity behavior of CW@PBD$_{15}$ and CW@PBD$_{25}$.

The magnetic parameters, as shown in Fig. S5 (ESI†), do not show significant change (μ' is around 0.2), because incorporation of trace amounts of PBD in CW@PBD$_{15}$ and CW@PBD$_{25}$ mainly plays the role of inducing graphitic carbon crystallization. In contrast, the increased PBD content in CW@PBD$_{35}$ endows the composite with a notable magnetic storage capacity. In addition, due to the enhanced conductivity of CW@PBD$_{25}$, the weak current generated by the magnetic field leads to a negative μ'', which impedes the action of the external magnetic field (Fig. S5b, ESI†).[43]

CW@PBD$_{15}$ and CW@PBD$_{25}$ demonstrate characteristics of a metacomposite, positioning them as promising candidates for EMI shielding applications. Therefore, the feasibility of CW@PBD$_{15}$ and CW@PBD$_{25}$ applied in EMI shielding was analyzed. Generally, when EMWs are incident on the surface of the EMI shielding materials, the EMWs are reflected due to the impedance matching. The impedance matching performance of CW, CW@PBD$_{15}$, and CW@PBD$_{25}$ can be evaluated using the transmission line theory (eqn (S10), ESI†).[43] As the value approached 0.8–1.2, the degree of impedance matching improved, and it was easier for the EMWs to enter the material.[44] The average value of $|Z_{in}/Z_0|$ for CW is 0.12, which indicates that CW has a certain level of EMI shielding performance (Fig. 5g). Loading with a trace amount of PBD NPs to induce graphitic carbon crystallization results in negative permittivity, and the average values of $|Z_{in}/Z_0|$ for CW@PBD$_{15}$ and CW@PBD$_{25}$ are less than 0.1, much less than 0.8–1. As a result, metacomposites with negative permittivity have impedance mismatch properties, leading to strong reflection of electromagnetic waves and contributing to achieving high EMI shielding effectiveness.[3]

3.4. EMI shielding performances of the CW@PBD metacomposites

The EMI shielding capabilities of the metacomposites within the 8.2–12.4 GHz are depicted in Fig. 6a. The total shielding effectiveness (SE$_T$) for the metacomposites rises substantially with an increased PBD NP content. All samples surpass the 20 dB EMI shielding effectiveness threshold. Specifically, the average SE$_T$ values for CW, CW@PBD$_{15}$, and CW@PBD$_{25}$ are recorded at 30.60 dB, 37.82 dB, and 39.13 dB, respectively. This enhancement is predominantly attributed to the pivotal role of conductivity in EMI shielding efficacy.[19] Incorporating PBD NPs catalyzes carbon graphitization, thereby establishing a more refined conductive network that facilitates the efficient movement of free carriers.

Interestingly, the reflection loss (SE$_R$) does not escalate with enhanced conductivity (Fig. 6b). The average SE$_R$ values for CW, CW@PBD$_{15}$, and CW@PBD$_{25}$ are 10.05 dB, 10.16 dB, and 10.17 dB, respectively. In contrast, the average absorption loss (SE$_A$) values for CW@PBD$_{15}$ and CW@PBD$_{25}$ are 27.66 dB and 28.96 dB, which represent an increase of 34.6% and 40.9% over CW (20.55 dB). This enhancement in SE$_A$ is primarily ascribed to dielectric loss. The energy of the incident wave is mitigated through conduction and polarization losses. Conduction loss occurs as electrons dissipate energy along the thin graphite structures, while polarization losses encompass both dipole and interface polarization. Dipolarization arises at defect sites, predominantly within the graphite layers. Under the influence of alternating high-frequency electromagnetic fields, the dipoles' motion falls out of sync with the field, leading to a loss of dipole polarization and the conversion of electromagnetic energy into heat.[45] Additionally, a trace amount of incorporated PBD can become a polarization focal point at heterogeneous interfaces, amplifying the polarization effect.[22] Concurrently, the porous nature of CW facilitates the elongation of the EMW propagation path within the material, thereby inducing reflection and scattering losses, which in turn attenuate the EMW.[15] The combined effect of these factors significantly boosts the SE$_A$ of CW@PBD$_{15}$ and CW@PBD$_{25}$. Notably, CW@PBD$_{25}$ exhibits an SE$_A$ that constitutes 74.1% of its SE$_T$ (Fig. 6c). It is important to clarify that a higher SE$_A$ than SE$_R$ does not imply an absorption-dominant shielding mechanism. The EMI shielding mechanism is dissected by calculating the power coefficient.[46] The reflection coefficients (R) for CW@PBD$_{15}$ and CW@PBD$_{25}$ are 0.9, while the absorption coefficients (A) are 0.09, indicating that the high conductivity predominantly drives a reflective EMI shielding mechanism, with the majority of the EMWs being reflected at the material's surface.[33]

Drawing from the findings, we delved into the potential EMI shielding mechanism of CW@PBD$_{25}$. The negative permittivity could provide the composites with an excellent conductive pathway. The increase in conductivity increases the conductive loss properties of the material to EMWs.[46] In addition, plasma oscillations occur in negative permittivity materials in the presence of electromagnetic fields. This process generates a reverse electric field inside the material, which results in the generation of counter-rotating EMWs to organize the propagation of EMWs.[3] The negative permittivity causes the EMW to convert into an evanescent field, thereby limiting the escape of the EMW.[47] The amplitude of the EMW grows exponentially with frequency, and thus the electromagnetic wave is consumed. Concurrently, the combination of negative permittivity and internal defects has been demonstrated to increase the induced current and polarization relaxation in the material.[39] This can increase the absorption loss of the material. In addition, the heterogeneous interface between the CW and PBD NPs causes substantial polarization losses that further attenuate the EMWs. Finally, the EMWs entering the interior of the material undergo multiple reflections and scattering losses in its three-dimensional network skeleton, which prolongs the propagation path of the EMWs.[21]
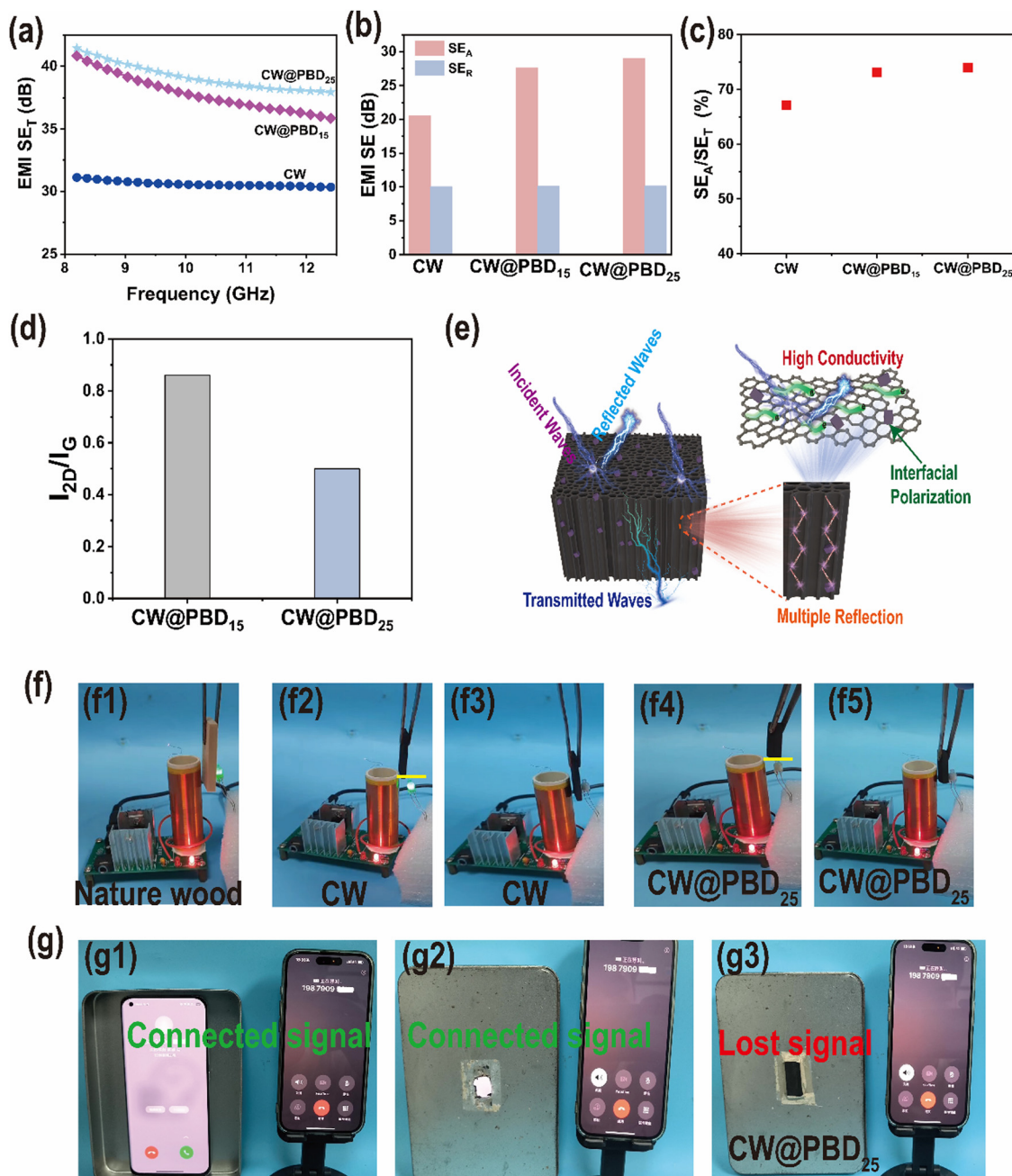
Fig. 6 EMI shielding performance of CW and CW@PBD. (a) EMI SE_T, (b) SE_A and SE_R, (c) SE_A/SE_T, (d) power coefficients, and (e) the EMI shielding mechanisms of CW@PBD$_{25}$. (f) Nature wood, CW, and CW@PBD$_{25}$ are applied for the wireless power system generated by the Tesla coil. (g) CW@PBD$_{25}$ is used in EMI shielding applications for mobile phone communications.

To visualize the EMI shielding performance of CW@PBD$_{25}$, its practical application was demonstrated (Fig. 6f and g). In a wireless power transmission system, a high-voltage electric field is generated around the Tesla coil when DC power is provided, causing the light bulb to illuminate. When natural wood is placed between the Tesla coil and the bulb, the bulb still lights (Fig. 6f1 and Video S1, ESI†). This suggests that natural wood cannot shield itself from EMWs. When CW is placed above the Tesla coil and the bulb (Fig. 6f2), the bulb is still light. The bulb goes out when the wood chip is replaced with CW (Fig. 6f3 and Video S2 ESI†). This means that CW

exhibits EMI shielding capability. In contrast, CW@PBD$_{25}$, no matter placed above or between the Tesla coil and the bulb, prevents the transmission of electromagnetic fields, causing the bulb to extinguish (Fig. 6f4, 5 and Video S3, ESI†). This observation underscores the superior EMI shielding performance of CW@PBD$_{25}$. Furthermore, a mobile phone is also placed in an EMI shielding box to evaluate its shielding potential in real-world scenarios. When the shielding box is opened, the signals from the two mobile phones can connect normally (Fig. 6g1, 2). When using CW@PBD$_{25}$ to seal the opening of the EMI shielding box, the signal of two

non-mobile phones cannot be successfully connected (Video S4, ESI†). This simple demonstration confirms the viability of employing CW@PBD$_{25}$ as an EMI shielding material across common frequency bands.

In order to realize the multi-scenario applicability of materials in complex electromagnetic environments, this study proposes a methodology for strengthening two complementary mechanisms of EMI shielding and microwave absorption through the induced design of magnetic particles. The former, represented by CW@PBD$_{25}$ metamaterials, relies on negative permittivity and polarization properties to attenuate EMW energy through interfacial reflection. The latter is exemplified by CW@PBD$_{35}$, which optimizes impedance matching with the assistance of magnetic nanoparticles. EMWs are induced to enter the interior of the material, where they undergo dielectric relaxation and hysteresis loss. The subsequent section is dedicated to the analysis of the microwave absorption properties and the mechanisms of the CW@PBD$_{35}$ composite.

3.5. High-efficiency microwave absorption properties of CW@PBD$_{35}$

Magnetic nanoparticles are often introduced into conductive materials to endow the materials with good microwave absorption properties.[48] PBD has excellent magnetism after high-temperature carbonisation and is often used as a microwave absorber.[43] Impedance matching ($|Z_{in}/Z_0|$) is a critical parameter for effective microwave absorption. Fig. 7a depicts the impedance matching for CW@PBD$_{35}$ across thicknesses ranging from 1.0 to 5.0 mm within the 8.2–12.4 GHz frequency. Notably, CW@PBD$_{35}$ demonstrates exceptional impedance matching for thicknesses between 2.5 and 5.0 mm, with $|Z_{in}/Z_0|$ values falling within the range of 0.8 to 1.0 across the entire X-band. This indicates that more EMWs can enter CW@PBD$_{35}$, where they are absorbed and dissipated.

The RL intensities were applied to describe the microwave absorption properties (eqn (S11) and (S12), ESI†).[25] Fig. 7b–d displays the RL$_{min}$ of CW@PBD$_{35}$ within 1.0–5.0 mm in the 8.2 to 12.4 GHz range. CW@PBD$_{35}$ exhibits excellent microwave absorption capabilities. The RL$_{min}$ was −49.2 dB at 11.8 GHz and 4.5 mm. Generally, an RL value ≤ -10 dB indicates that $\geq 90\%$ of the incident EMW can be dissipated. The corresponding bandwidth can be defined as effective absorption bandwidth (EAB). The EAB of CW@PBD$_{35}$ is 4.2 GHz, covering the entire X-band. These exceptional EMW absorption characteristics stem from the synergistic interaction of electromagnetic parameters. Consequently, the magnetic loss properties of CW@PBD$_{35}$ were assessed, and its potential absorption mechanism was dissected. The eddy current loss coefficient (Co) values vary little over the test frequency range, and thus most of the resulting magnetic loss comes from the eddy current loss of the PBD NPs (Fig. S6b, ESI†).

The superior microwave absorption of CW@PBD$_{35}$ stems from its multi-scale synergistic dissipation mechanisms (Fig. 7e). The PBD NPs loaded on the CW surface create abundant heterogeneous interfaces, inducing interfacial polarization to attenuate EMWs.[48] Simultaneously, structural defects formed during
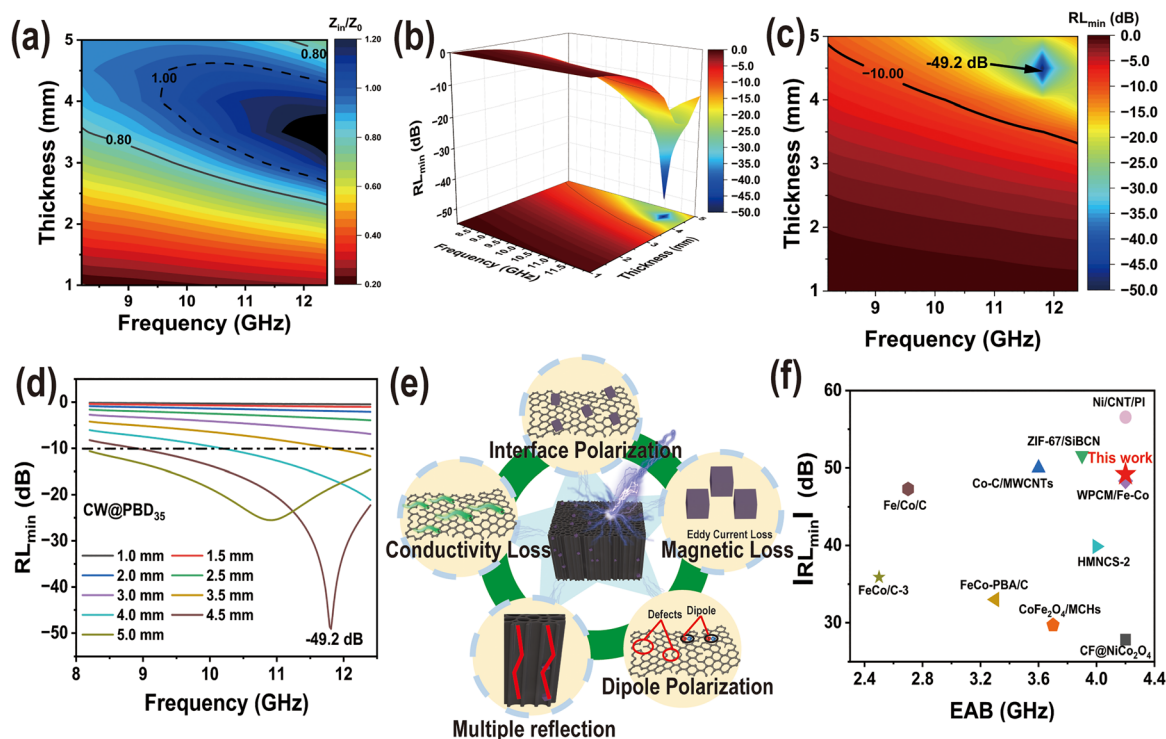

Fig. 7 Microwave absorption performance of CW@PBD$_{35}$. (a) Impedance matching, (b)–(d) 3D and 2D plots of reflection loss and reflection loss curves, (e) schematic diagram of the microwave absorption mechanism, and (f) comparison of X-band microwave absorption performance from the aspects of EAB and |RL$_{min}$| (ref. S3–S12, ESI†).

graphitization act as dipolar polarization centers, generating dipolar polarization loss under alternating electromagnetic fields.[31] The moderate conductivity enables conductive currents that trigger ohmic loss, converting electromagnetic energy into heat.[17] Additionally, magnetic nanoparticles enhance wave attenuation through magnetic hysteresis and eddy current losses.[19] Crucially, the porous framework of CW extends EMW propagation paths *via* multi-reflection and scattering effects, progressively dissipating incident waves through repeated interactions.[49] This coordinated "polarization relaxation–conduction loss–geometric dissipation" system ensures efficient electromagnetic energy absorption and conversion. Therefore, the excellent microwave absorption performance of CW@PBD$_{35}$ is attributed to the multiple synergistic loss mechanism.

The performance of CW@PBD$_{35}$ prepared in this work was compared with that of recently reported advanced microwave absorbing materials in the X-band (Fig. 7f and Table S1, ESI†). Compared to microwave-absorbing materials reported in the literature, CW@PBD$_{35}$ exhibits high EMW absorption performance (−49.2 dB) across a relatively broad EAB (4.2 GHz). CW@PBD$_{35}$ shows great potential to be an efficient and inexpensive EMW absorber.

3.6. Joule heating performance of the CW@PBD$_{25}$ metacomposite

In addition, CW@PBD was explored as an effective electrical heater. Herein, the CW@PBD$_{25}$ metacomposite, which exhibits optimal conductivity, was utilized as an electric heater to assess its Joule heating performance. The nearly linear *V–I* curve in
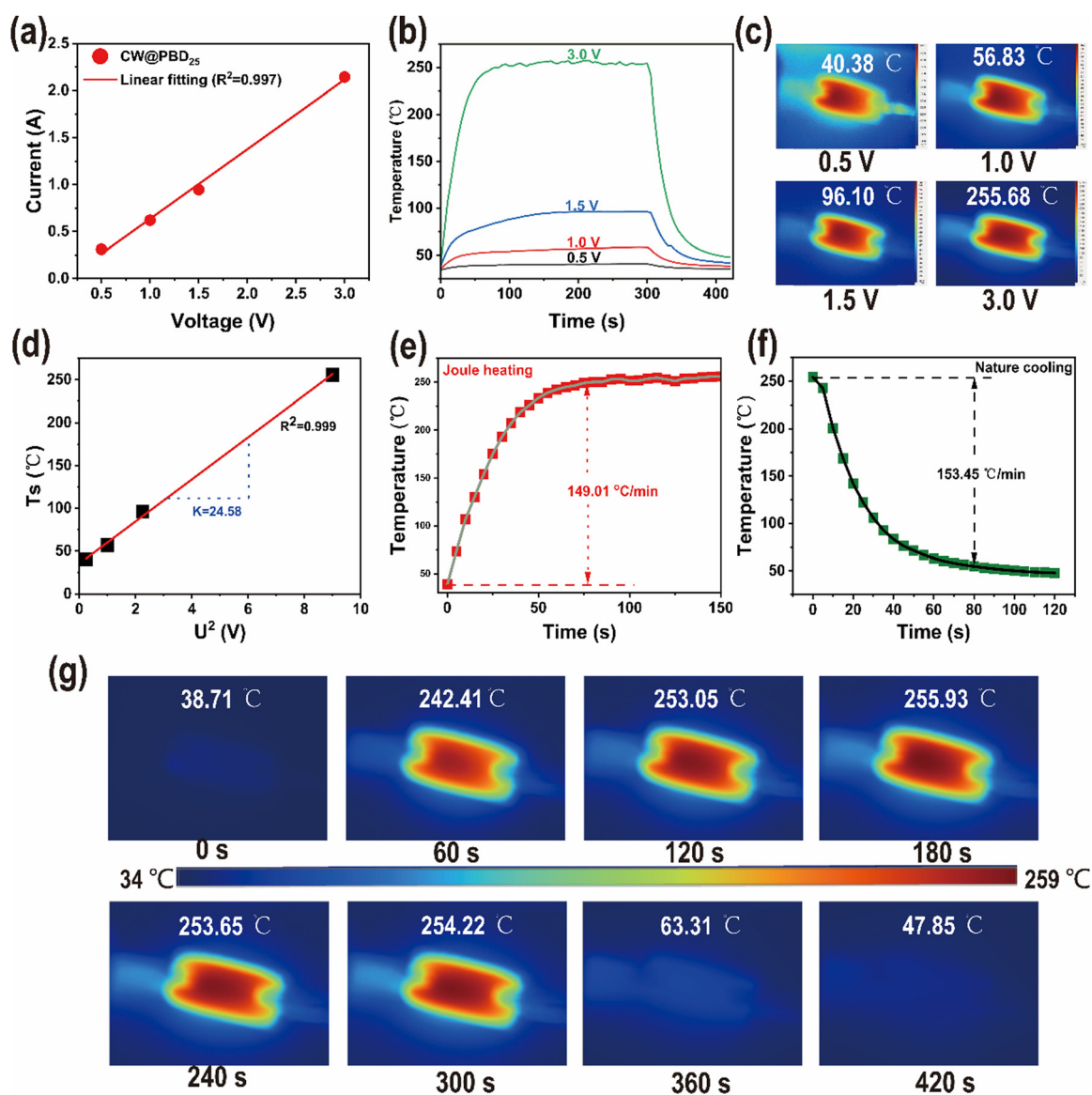

Fig. 8 Joule heating performance. (a) *V–I* curve, (b) temperature profiles of CW@PBD$_{25}$ at different voltages, (c) infrared image of the temperature region of CW@PBD$_{25}$ at different voltages, (d) *U*^{2}–*T* curve, (e) and (f) heating and cooling process of CW@PBD$_{25}$ at 3.0 V, and (g) infrared image of the temperature region of CW@PBD$_{25}$ at 3.0 V with different times.

Fig. 8a shows that the resistance of CW@PBD$_{25}$ is extremely low, which can ensure stability and safety during the heating process at a low working voltage. Fig. 8b displays the time-dependent surface temperature of CW@PBD$_{25}$ with different supplied voltages (0.5–3.0 V). As the working voltage rises, the surface steady-state saturated temperature (T_s) improves drastically, ascribed to more Joule heat power produced from the composite material.[50] At a voltage of 3.0 V, the T_s of CW@PBD$_{25}$ quickly exceeds the high temperature of 255.68 °C within 60 s, thanks to an improved graphite structure that forms a highly conductive network. Notably, all the T_s will be reached within 60 s regardless of the high or low voltage applied, demonstrating rapid responses for the electrical heaters. The thermodynamic evaluation of the heating response for CW@PBD$_{25}$ was conducted to further investigate the mechanism for the observed Joule heating performance. According to the energy balance principle, the temperature of electronics would be equilibrated when the dissipated power by Joule heating becomes equal to the power losses *via* radiation, convection, and conduction.[51] Specifically, the temperature could be obtained using the following equation:

$$\frac{U^2}{R} = mc\frac{dT}{dt} + hA(T - T_0) \tag{5}$$

where U is the working voltage, R is the resistance of the heating device, m is the mass of the composite, c is the specific heat capacity, h is the convective heat-transfer coefficient, A is the area of the electrical heater, T is the surface temperature of the electrical heater, and T_0 is the ambient temperature respectively. Combining eqn (5) and considering that $T_{(t=0)} = T_0$, the real-time temperature and T_s of this heater would be obtained respectively as follows:

$$T = T_0 + \frac{U^2}{RhA}\left(1 - e^{-(hA/mc)t}\right) \tag{6}$$

$$T_s = T_0 + \frac{U^2}{RhA} \tag{7}$$

From these equations, it is clear that the square of the resistance, convective heat-transfer coefficient resistance, and driving voltage of the electronics govern the T_s of the device. Moreover, Fig. 8d shows the experimental data and the linear fitting of T_s *versus* U^2. Note that the as-prepared CW@PBD$_{25}$ exhibits an excellent linear relationship with the square of the supplied voltage ($R^2 = 0.999$), indicating the accuracy of the theoretical prediction of saturation temperature at different working voltages, by previous reports.[52] Moreover, infrared (IR) images clearly show uniform temperature distribution of CW@PBD$_{25}$ at different applied voltages, as illustrated in Fig. 8c. Fig. 8g depicts the thermal infrared map during the ramp-up constant-temperature-down process at CW@PBD$_{25}$ with a voltage of 3.0 V. Beyond the T_s, the heating and cooling rates are pivotal in assessing the performance of the Joule heater. At 3.0 V, the heating rates for CW@PBA$_{25}$ were 149.01 °C min^{-1}, and the cooling rates were 153.45 °C min^{-1}.

Both the heating rate and cooling rate of CW@PBA$_{25}$ exceeded the values reported for a carbon nanogel (234 K min^{-1} and 294 K min^{-1}).[53] In order to evaluate the stability and reliability of the CW@PBD25 composite under long-term operating conditions, Fig. S7 (ESI†) shows the temperature changes *versus* time at a constant input voltage of 3.0 V. The Joule heating performance demonstrated no significant change following several heating cycles. Meanwhile, the CW@PBD$_{25}$ composite exhibits an excellent stable temperature of about 255 °C within 900 s after voltage input. This demonstrates the stability and reliability of CW@PBD$_{25}$ composites when it comes to cycling and long-term use. A comparison of various Joule heaters reported in the literature is provided in Table S2 (ESI†). The Joule heating performance of CW@PBD$_{25}$ Joule heaters surpasses that of many previously reported Joule heaters, including those based on CW and its composites, carbon nanotubes, silver nanowire composites, MXene composites, and metal particle composites. A CW@PBD$_{25}$ Joule heater can achieve a high Joule heating temperature (255 °C) at 3.0 V. Therefore, its outstanding performance bodes well for its great application prospects.

4. Conclusion

In conclusion, the CW@PBD metacomposites were successfully synthesized with varying PBD NP contents by high-temperature carbonization. Metacomposites have a thinner and more complete graphite structure, which allows them to undergo plasma oscillations in the X-band, resulting in a negative permittivity behavior. The Drude model provides a full explanation of this behavior. The SE$_T$ of the CW@PBD$_{25}$ metacomposite is 39.1 dB, while the SE$_A$ demonstrates a 40.9% increase. In addition, the impedance matching performance of CW@PBD$_{35}$ has been optimised by increasing the content of PBD magnetic nanoparticles. The microwave absorption capability of CW@PBD$_{35}$ is enhanced by the synergistic effect of multiple loss mechanisms, resulting in an RL$_{min}$ = −49.2 dB and the EAB covers the X-band. CW@PBD$_{25}$ has excellent Joule heating properties (T_s = 255 °C at 3.0 V). This work provides new insights into the design of materials with negative dielectric constants and EMI shielding materials.

Author contributions

Chenchen Wang: methodology, formal analysis, data curation, and writing – original draft. Xiuyi Lin: visualization and project administration. Chuanshuang Hu: supervision and project administration. Yao Ding: investigation. Zhuoqun Wang: investigation. Yonghui Zhou: investigation and formal analysis. Xi Lin: investigation. Jiangtao Xu: resources, project administration, and writing – review & editing.

Data availability

The raw data supporting the conclusions of this article will be made available by the authors on request.

Conflicts of interest

The authors declare no conflicts of interest. They have no known competing financial interests or personal relationships that could have appeared to influence the work reported in this paper.

Acknowledgements

References

1 R. Shelby, D. Smith and S. Schultz, *Science*, 2001, **292**, 77–79.

2 D. Schurig, J. Mock, B. Justice, S. Cummer, J. Pendry, A. Starr and D. Smith, *Science*, 2006, **314**, 977–980.

3 J. Bi, Z. Sun, Z. Guo, S. Tian, G. Li and L. Qian, *J. Mater. Chem. C*, 2024, **12**, 13974–13984.

4 H. Wu, Z. Zhang, C. Wang, K. Abualnaja, H. Abo-Dief, Q. Hou, H. Algadi, R. Yin, X. Liu, P. Xie and Y. Liu, *Adv. Compos. Hybrid Mater.*, 2023, **6**, 206.

5 B. Li, G. Sui and W.-H. Zhong, *Adv. Mater.*, 2009, **21**, 4176–4180.

6 A. Boltasseva and H. A. Atwater, *Science*, 2011, **331**, 290–291.

7 K. Sun, C. Wang, J. Tian, Z. Zhang, N. Zeng, R. Yin, W. Duan, Q. Hou, Y. Zhao, H. Wu and R. Fan, *Adv. Funct. Mater.*, 2024, **34**, 2306747.

8 Z. Wang, K. Yin, Y. Zhang, K. Sun, L. Xie, M. Cong, S. Cao, Y. Lei, X. Li and R. Fan, *Adv. Compos. Hybrid Mater.*, 2022, **5**, 2369–2377.

9 C. Cheng, Y. Liu, R. Ma and R. Fan, *Composites, Part A*, 2022, **155**, 106842.

10 Z. Wang, K. Sun, P. Xie, Q. Hou, Y. Liu, Q. Gu and R. Fan, *Acta Mater.*, 2020, **185**, 412–419.

11 Z. Guo, A. Li, Z. Sun, Z. Yan, H. Liu and L. Qian, *Adv. Compos. Hybrid Mater.*, 2022, **5**, 50–57.

12 P. Quan, C. Long, J. Zhou, X. He, Y. Liu, D. DeVallance, X. Li and X. Xie, *Holzforschung*, 2022, **76**, 368–379.

13 C. Xiong, T. Wang, Y. Zhang, M. Zhu and Y. Ni, *Nano Res.*, 2022, **15**, 7506–7532.

14 Z. Dai, C. Hu, Y. Wei, W. Zhang, J. Xu and X. Lin, *Adv. Electron. Mater.*, 2023, **9**, 2300162.

15 C. Liang, H. Qiu, P. Song, X. Shi, J. Kong and J. Gu, *Sci. Bull.*, 2020, **65**, 616–622.

16 B. Zhao, P. Bai, S. Wang, H. Ji, B. Fan, R. Zhang and R. Che, *ACS Appl. Mater. Interfaces*, 2021, **13**, 29101–29112.

17 X. Hao, D. Li, X. Peng, W. Lan and C. Liu, *Chem. Eng. J.*, 2024, **479**, 147681.

18 Y. Wang, H. Ren, C. Cheng, C. Xu, G. Fan and Y. Liu, *ECS J. Solid State Sci. Technol.*, 2020, **9**, 83001.

19 Z. Dai, C. Hu, Y. Li, Z. Wang, Y. Wei, W. Zhang, J. Xu, S. Fu and X. Lin, *ACS Appl. Nano Mater.*, 2023, **6**, 13646–13655.

20 C. Thambiliyagodage, S. Ulrich, P. Araujo and M. Bakker, *Carbon*, 2018, **134**, 452–463.

21 J. Huang, H. Wan, M. Li, Y. Zhang, J. Zhu, X. Li, W. Shui, Y. Li, X. Fan, Q. Wen, X. Xiao and Q. Huang, *J. Adv. Ceram.*, 2021, **10**, 1291–1298.

22 M. Cheng, W. Ren, H. Li, X. Liu, S. Bandaru, J. Zhang and X. Zhang, *Composites, Part B*, 2021, **24**, 109169.

23 S. Wei, T. Chen, Z. Shi and S. Che, *J. Colloid Interface Sci.*, 2022, **610**, 395–406.

24 J. Zhang, N. Kong, D. Hegh, K. A. S. Usman, G. Guan, S. Qin, I. Jurewicz, W. Yang and J. M. Razal, *ACS Appl. Mater. Interfaces*, 2020, **12**, 34032–34040.

25 F. Li, N. Wu, H. Kimura, Y. Wang, B. B. Xu, D. Wang, Y. Li, H. Algadi, Z. Guo, W. Du and C. Hou, *Nano-Micro Lett.*, 2023, **15**, 220.

26 X. Hu, J. Wang, J. Wang, D. Yao, H. Zhang, T. Xu and W. Wang, *Appl. Catal., B*, 2022, **318**, 121879.

27 F. Li, Q. Li, H. Kimura, X. Xie, X. Zhang, N. Wu, X. Sun, B. B. Xu, H. Algadi, R. Pashameah, A. Alanazi, E. Alzahrani, H. Li, W. Du, Z. Guo and C. Hou, *J. Mater. Sci. Technol.*, 2023, **148**, 250–259.

28 C. Xu, L. Wang, X. Li, X. Qian, Z. Wu, W. You, K. Pei, G. Qin, Q. Zeng, Z. Yang, C. Jin and R. Che, *Nano-Micro Lett.*, 2021, **13**, 47.

29 F. Chen, S. Zhang, B. Ma, Y. Xiong, H. Luo, Y. Cheng, X. Li, X. Wang and R. Gong, *Chem. Eng. J.*, 2022, **43**, 134007.

30 W. Hou, Q. Liao, M. Wu, K. Liao, Y. Song and L. Qin, *J. Alloys Compd.*, 2023, **937**, 168283.

31 M. Wang, S. Ji, H. Wang, V. Linkov, X. Wang and R. Wang, *J. Power Sources*, 2023, **571**, 233069.

32 G. Jia, Y. Yu, X. Wang, C. Jia, Z. Hu, S. Yu, H. Xiang and M. Zhu, *Mater. Horiz.*, 2023, **10**, 5847–5858.

33 T. Gao, Y. Ma, L. Ji, Y. Zheng, S. Yan, Y. Li and X. Zhang, *Adv. Compos. Hybrid Mater.*, 2022, **5**, 2328–2338.

34 T. Nakamura, H. Gao, K. Ohta, Y. Kimura, Y. Tamenori, K. Nitta, T. Ina, M. Oishi and K. Amezawa, *J. Mater. Chem. A*, 2019, **7**, 5009–5019.

35 K. Sun, J. Dong, Z. Wang, Z. Wang, G. Fan, Q. Hou, L. An, M. Dong, R. Fan and Z. Guo, *J. Phys. Chem. C*, 2019, **123**, 23635–23642.

36 T. Iwasaki, T. Zelai, S. Ye, Y. Tsuchiya, H. Chong and H. Mizuta, *Carbon*, 2017, **111**, 67–73.

37 C. Wang, X. Tang, Z. Zhang, K. Sun, G. Liang, K. Zheng, N. Zeng, Z. Mao, J. Song and R. Fan, *Adv. Compos. Hybrid Mater.*, 2024, **7**, 4.

38 J. Zeng, W. Xie, H. Zhou, T. Zhao, B. B. Xu, Q. Jiang, H. Algadi, Z. Zhou and H. Gu, *Adv. Compos. Hybrid Mater.*, 2023, **6**, 64.

39 C. Cheng, Y. Jiang, X. Sun, J. Shen, T. Wang, G. Fan and R. Fan, *Composites, Part A*, 2020, **130**, 105753.

40 J. Chen, Y. Wang, Z. Gu, J. Huang, W. He and P. Liu, *Carbon*, 2023, **204**, 305–314.

41 X. Li, R. Hu, Z. Xiong, D. Wang, Z. Zhang, C. Liu, X. Zeng, D. Chen, R. Che and X. Nie, *Nano-Micro Lett.*, 2024, **16**, 42.

42 T. Zhao, Z. Jia, J. Liu, Y. Zhang, G. Wu and P. Yin, *Nano-Micro Lett.*, 2024, **16**, 6.

43 J. Wang, S. Zhang, Z. Liu, T. Ning, J. Yan, K. Dai, C. Zhai and J. Yun, *J. Colloid Interface Sci.*, 2023, **652**, 2029–2041.

44 W. Cui, X. Zhou, B. Zhao, W. You, Y. Yang, B. Fan, L. Wu and R. Che, *Carbon*, 2023, **210**, 118070.

45 G. Li, Z. Sun, Z. Guo, P. Wang, B. Du, S. Tian, H. Ding, Y. Qiu, J. Bi and L. Qian, *Adv. Compos. Hybrid Mater.*, 2024, **7**, 83.

46 X. Ma, J. Pan, H. Guo, J. Wang, C. Zhang, J. Han, Z. Lou, C. Ma, S. Jiang and K. Zhang, *Adv. Funct. Mater.*, 2023, **33**, 2213431.

47 D. Smith, W. Padilla, D. Vier, S. Nemat-Nasser and S. Schultz, *Phys. Rev. Lett.*, 2000, **84**, 4184–4187.

48 C. Wang, C. Hu, Y. Ding, Z. Li, Z. Wang, X. Lin, Y. Zhou and J. Xu, *ACS Appl. Mater. Interfaces*, 2025, **17**, 2048–2062.

49 J. Xi, E. Zhou, Y. Liu, W. Gao, J. Ying, Z. Chen and C. Gao, *Carbon*, 2017, **124**, 492–498.

50 J. Flores Cuautle, R. Martínez Valdez, E. Rodríguez Carmona, R. Posada Gomez and C. Trujillo Romero, *J. Therm. Biol.*, 2021, **97**, 102868.

51 Y. An, C. Li and X. Sheng, *Nanoscale*, 2019, **11**, 17073–17083.

52 X. Zhao, L. Wang, C. Tang, X. Zha, Y. Liu, B. Su, K. Ke, R. Bao, M. Yang and W. Yang, *ACS Nano*, 2020, **14**, 8793–8805.

53 D. Xia, H. Li, C. Shen and P. Huang, *ACS Appl. Nano Mater.*, 2023, **6**, 7532–7542.